Modification of turbulent dissipation rates by a deep Southern Ocean eddy

K. L. Sheen[1], J. A. Brearley[1,2], A. C. Naveira Garabato[1], D. A. Smeed[3], L. St. Laurent[4], M. P. Meredith[5,2], A. M. Thurnherr[6], and S. N. Waterman[7]

[1]Ocean and Earth Sciences, University of Southampton, Southampton, UK, [2]British Antarctic Survey, Cambridge, UK, [3]National Oceanography Centre, Southampton, UK, [4]Woods Hole Oceanographic Institution, Woods Hole, Massachusetts, USA, [5]Scottish Association for Marine Science, Oban, UK, [6]Lamont-Doherty Earth Observatory, Palisades, New York, USA, [7]University of British Columbia, Vancouver, British Columbia, Canada

Abstract The impact of a mesoscale eddy on the magnitude and spatial distribution of diapycnal ocean mixing is investigated using a set of hydrographic and microstructure measurements collected in the Southern Ocean. These data sampled a baroclinic, middepth eddy formed during the disintegration of a deep boundary current. Turbulent dissipation is suppressed within the eddy but is elevated by up to an order of magnitude along the upper and lower eddy boundaries. A ray tracing approximation is employed as a heuristic device to elucidate how the internal wave field evolves in the ambient velocity and stratification conditions accompanying the eddy. These calculations are consistent with the observations, suggesting reflection of internal wave energy from the eddy center and enhanced breaking through critical layer processes along the eddy boundaries. These results have important implications for understanding where and how internal wave energy is dissipated in the presence of energetic deep geostrophic flows.

1. Introduction

Subsurface mesoscale eddies have been observed throughout the oceans. The best known examples are the lenses of warm, salty Mediterranean Water (MW) known as Meddies, whose long lifetimes enable the transport of MW as far west as the Bahamas, modifying the water mass properties of the subtropical North Atlantic [*McDowell and Rossby*, 1978; *Richardson et al.*, 2000]. More recently, a number of anticyclonic middepth eddies were identified in the Scotia Sea sector of the Southern Ocean [*Brearley et al.*, 2014]. The stability of these eddies, which are advected into the highly energetic Antarctic Circumpolar Current (ACC), may explain why the distinct T/S and oxygen fingerprint of the Pacific Deep Water is traceable for thousands of kilometers downstream of Drake Passage [*Well et al.*, 2003].

In addition to being an important mechanism by which heat, salt, and nutrients are dispersed over large distances, subsurface eddies may also strongly impact the local shear-driven diapycnal mixing. Having typical diameters of 10–100 km, these features modify the ambient velocity shear and stratification fields, which affect the propagation and breaking of local internal waves. However, direct measurements of turbulent shear within such features remain scarce, with the few studies that do exist describing an enhancement of turbulent mixing in the periphery of subsurface eddies, alongside a suppression of mixing within the eddy core [e.g., *Armi et al.*, 1988; *Sheen et al.*, 2009; *Forryan et al.*, 2012]. Understanding how subsurface eddies affect the underlying temporal and spatial distributions of internal wave breaking and diapycnal diffusivity is particularly important in the eddy-rich Southern Ocean. Here diapycnal processes are known to be important in the transformation of water masses and the closure of the oceanic meridional overturning circulation [*Marshall and Speer*, 2012; *Watson et al.*, 2013].

In this study we analyze a set of opportunistic microstructure, hydrographic, and current velocity measurements collected under the auspices of DIMES (the Diapycnal and Isopycnal Mixing Experiment in the Southern Ocean). From these data, a deep anticylonic eddy was identified in the northern Scotia Sea to the east of Drake Passage (Figure 1). Further data collected in the same region 2 weeks later showed that the eddy had migrated away. The presence of the eddy was found to significantly modify local turbulent dissipation rates. Because the distribution of turbulent mixing in the ACC is believed to be primarily controlled by the generation and breaking of internal waves [*Waterman et al.*, 2012; *Sheen et al.*, 2013; *Brearley et al.*, 2013], a simple ray tracing model of internal wave propagation was employed as a first step in elucidating how
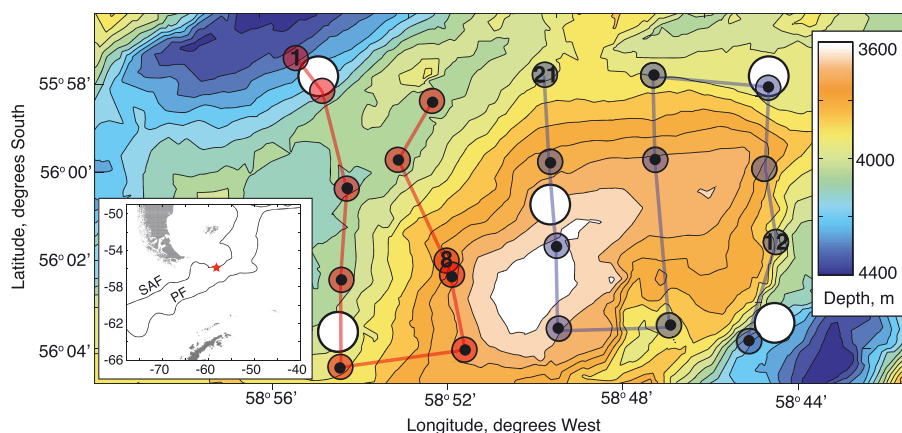
Figure 1. Map of grid survey, with topography shown in color. CTD and LADCP stations are indicated by colored circles, while the locations of the five moorings are shown by white circles. Stations with small black circles indicate that a VMP was also deployed. The western stations (in red), in particular stations 1–6, correspond to stations in which the eddy is present. The inset shows the location of the grid survey close to 56°S, 59°W (red star) relative to South America and the Antarctic Peninsula. The mean positions of the Subantarctic Front (SAF) and Polar Front (PF), from *Orsi et al.* [1995], are indicated.

internal waves may evolve in the presence/absence of the middepth eddy. Our observations indicate that while the eddy decay timescale is likely to be controlled by isopycnal processes, the feature significantly influences both the internal wave field and the distribution of diapycnal mixing in the surrounding waters.

2. Data

A spatial grid of 21 conductivity-temperature-depth (CTD) and Lowered Acoustic Doppler Current Profiler (LADCP) stations was occupied over a 10 km × 10 km topographic feature east of Drake Passage in the Antarctic Circumpolar Current (Figure 1). Fifteen of the stations were accompanied by the deployment of a full-depth free-falling vertical microstructure profiler (VMP), which recorded direct estimates of the rate of turbulent energy dissipation, ϵ. These data were collected as part of DIMES between 5 and 22 December 2010 on the RRS *James Cook* during the turnaround of a colocated five-element mooring array [*Brearley et al.*, 2013]. The CTD and LADCP measurements were interspersed between VMP deployment and recovery. Two Rockland Scientific International VMP-5500 instruments were used during the survey. Profiler drift was rarely more than a few kilometers, and at most stations, data were collected to within 100 m of the seafloor [*Sheen et al.*, 2013].

The fine-scale CTD and LADCP measurements were used to produce depth profiles of temperature, salinity, buoyancy frequency, and current velocities and to characterize the local internal wavefield. Shear-to-strain ratios, R_ω, indicate the predominant frequency content of the internal wavefield, ω, through the relationship $(\omega/f)^2 \cong (R_\omega + 1)/(R_\omega - 1)$, where f is the Coriolis frequency [*Polzin et al.*, 2014]. The counterclockwise, CCW, and clockwise, CW, rotary vertical shear variances, which indicate the dominant direction of internal wave propagation, were also estimated. Full details of the analysis used to compute these parameters, alongside CTD, LADCP, and VMP processing and accuracies, are given in *Sheen et al.* [2013].

3. Observations
3.1. Eddy Characteristics
Brearley et al. [2014] used these CTD and LADCP data to show that a middepth anticyclonic eddy was captured on the western part of the grid survey (stations 1–6, collected on 7–10 December 2010). The eddy was distinguished by ~1 km thick intensification in LADCP current speeds centered at 2000 m (Figure 2); pronounced isopycnal separation between neutral density surfaces $\gamma^n = 27.85$ kg m^{-3} and $\gamma^n = 28.00$ kg m^{-3} (Figure 2); a local minimum in potential vorticity; pronounced cooling and freshening (0.1°C and 0.02, respectively) along isopycnal surfaces; and an oxygen concentration minimum. Analysis of similar features captured by the colocated mooring array showed that 9 such features crossed the grid location over a 26 month period. Typically, the eddies had radii of 10–30 km, Rossby numbers of 0.1–0.3, and azimuthal velocities of 0.25–0.4 m s^{-1}. The eddies were likely sourced from instabilities in the boundary current that flows along the western slope of
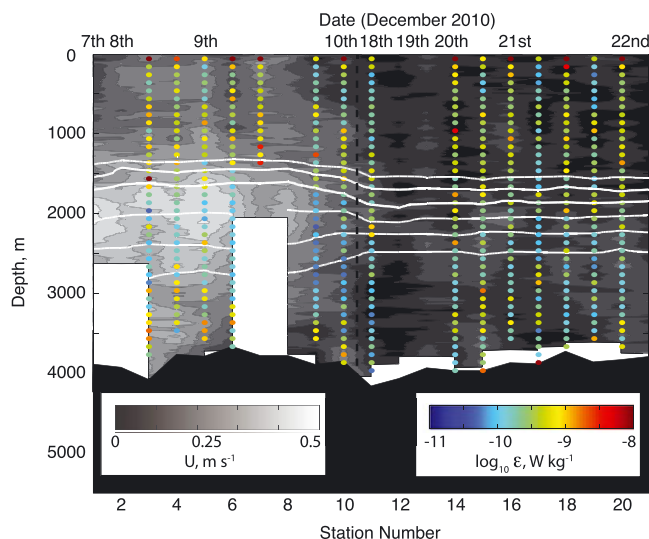
Figure 2. Current speed, U, and turbulent dissipation rates, ϵ, across the grid survey. Gray contours show background speed as measured by the LADCP, and colored dots indicate dissipation estimates from microstructure casts, depth averaged into 100 m bins. White lines show neutral density levels at 0.05 kg m^{-3} intervals between 27.75 kg m^{-3} and 28.0 kg m^{-3} and correspond to the dashed horizontal lines in Figure 3. The vertical black dashed line highlights the large time gap between the two groups of stations.

South America and northern continental slope of Drake Passage. In contrast, the eddy was not present in stations 11–21, which were collected 11 days later in the eastern half of the grid (Figure 2). Note that throughout the text we refer to the vertical center of the eddy as the eddy core, as we have not necessarily resolved the horizontal eddy center.

3.2. Turbulent Dissipation Rates

Microstructure estimates of turbulent dissipation in the grid survey show a striking suppression of dissipation within the eddy core ($\epsilon \sim 1 \times 10^{-10}$ W kg^{-1}), alongside an enhancement in dissipation around the top and bottom eddy boundaries where average ϵ values reach 10×10^{-10} W kg^{-1} (stations 3–6, Figures 2 and 3b). In contrast, the absence of the eddy yields dissipation rates that are more uniform, being consistently around $1.5 - 3 \times 10^{-10}$ W kg^{-1} below 500 m depth (stations 11–21).

3.3. Internal Wave Frequency Content

At the center of the eddy core (2000 m, $\gamma_n = 27.90$ kg m^{-3}), which is associated with a stratification minimum and a speed maximum, shear-to-strain ratios indicate that internal wavefield frequencies peak and approach
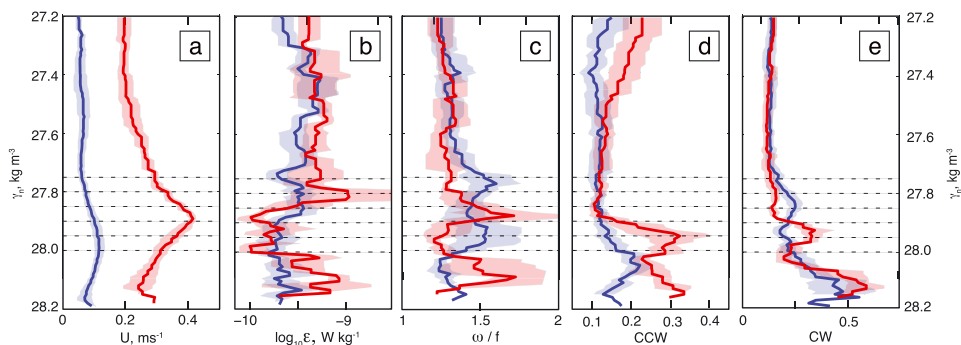
Figure 3. Observed properties averaged across eddy (red, stations 3–6) and noneddy (blue, stations 14–20) profiles (only CTD stations with concurrent VMP measurements are included). (a) Current speed, U. (b) Microstructure dissipation estimates, ϵ. (c) Dominant frequency content of the internal wavefield, computed using shear-to-strain ratios, ω/f. (d) Downward propagating component of the shear variance, CCW. (e) Upward propagating component of the shear variance, CW. The shaded regions show the 95% confidence interval in mean values, calculated by bootstrapping.

the local buoyancy frequency, N (Figure 3c). In contrast, at the top and bottom edges of the eddy, internal wave frequencies are lower than at times when the eddy is absent and approach the Coriolis frequency, f.

3.4. Direction of Internal Wave Energy Propagation

In the upper half of the eddy core (1500–2000 m, γ_n: 27.75–27.90 kg m^{-3}), the presence of the eddy has little effect on the downward propagating internal wave energy. However, the upward energy propagation is marginally suppressed in this region (Figures 3d and 3e).

Both CW (upward propagating) and CCW (downward propagating) polarized internal wave energies show enhancement within the bottom half of the eddy core (2000–2800 m, γ_n: 27.90–28 kg m^{-3}) compared with when the eddy is absent. This signal is accompanied by low strain variances and hence high shear-to-strain ratios, as noted above. Despite an increase in both the CCW and CW, the signal is strongest in the CCW component, particularly at depths below 3000 m ($\gamma_n = 28$ kg m^{-3}), i.e., in the region below the base of the eddy. These observations are apparent at vertical wavelengths between 60 m and 500 m (Figures 4a and 4b), although LADCP data noise at higher wave numbers limits what can be concluded.

3.5. Wave-Mean Flow Interactions

The vertical internal wave energy flux and the integrated turbulent energy dissipation match each other well in both the eddy and noneddy regions (Figures 4c and 4d). This result indicates that the majority of the internal wave energy around the eddy is transferred to turbulent dissipation and mixing, probably through critical layer interactions, as opposed to being lost to the mean flow. There is a hint of excess wave energy flux convergence compared to the turbulent energy dissipation in the upper and lower eddy core (1700–1900 m and 2700–2800 m). This difference may simply reflect the poorer vertical resolution of wave energy flux values but could indicate that some energy exchange is occurring with the background flow at these locations. Richardson numbers, computed over 100 m vertical scale, are found to be greater than unity throughout the eddy, indicating that most of the wave motion is likely to be absorbed by a critical layer [*Booker and Bretherton*, 1967].

3.6. Summary of Observations

In summary, turbulent-scale shear measurements show that turbulent kinetic energy dissipation is suppressed within the eddy core, reaches a maximum at the eddy upper boundary, and is also significantly enhanced beneath the eddy. Shear-to-strain ratios indicate a progressive reduction in internal wave frequencies from the surrounding water toward the eddy core, although a peak in internal wave frequency content is observed at the very center of the eddy. The presence of the eddy is also associated with enhanced downward propagating internal wave energy between the eddy core and seabed and an apparent suppression of upward propagating energy above the eddy core. Finally, wave energy fluxes are broadly consistent with measured dissipation rates. These observations point toward the eddy acting to deflect internal wave breaking away from the eddy core to the surrounding water and to trap bottom sourced, upward propagating internal waves between the eddy core and the seabed. In the next section, we employ a ray tracing model to investigate further the possible influence of the eddy on the local internal wave evolution.

4. Ray Tracing Calculations

The propagation of internal wave packets, and the evolution of their properties along a ray path for a specified background stratification and velocity field, may be mapped using ray tracing techniques [e.g., *Lighthill*, 1978; *Olbers*, 1981; *Bühler and McIntyre*, 1999]. Internal wave rays are both advected by the mean horizontal current, $U(z)$, and distorted by the local vertical current shear, U_z, and background stratification gradient, N_z. Here we conduct a linear ray tracing experiment in two spatial dimensions: the zonal dimension, x, and depth, z. We model the mean current as a steady zonal flow, which varies in depth, $U(z)$. Similarly, a constant buoyancy frequency-depth profile, $N(z)$, is employed, and a Coriolis parameter, f, of 1.2×10^{-4} rad s^{-1} is assumed. In this simple model we choose to ignore the relative vorticity of the eddy (typically 0.3×10^{-4} rad s^{-1} [*Brearley et al.*, 2014]), which locally is significantly smaller than f. Two models are run, which differ only by the background $U(z)$ and $N(z)$ profiles, and are chosen to be representative of eddy and noneddy scenarios (Figures 5a and 5b). The profiles are computed from averaged LADCP and CTD data for eddy (stations 3–6) and noneddy (stations 14–20) times. The $U(z)$ profiles are smoothed using a running average over 100 m, and the $N(z)$ are profiles computed using adiabatic leveling over a pressure range of 400 dbar [*Bray and Fofonoff*, 1981]. We choose to discard the upper 500 m where U and N are known to vary in the horizontal on a broad range of scales.
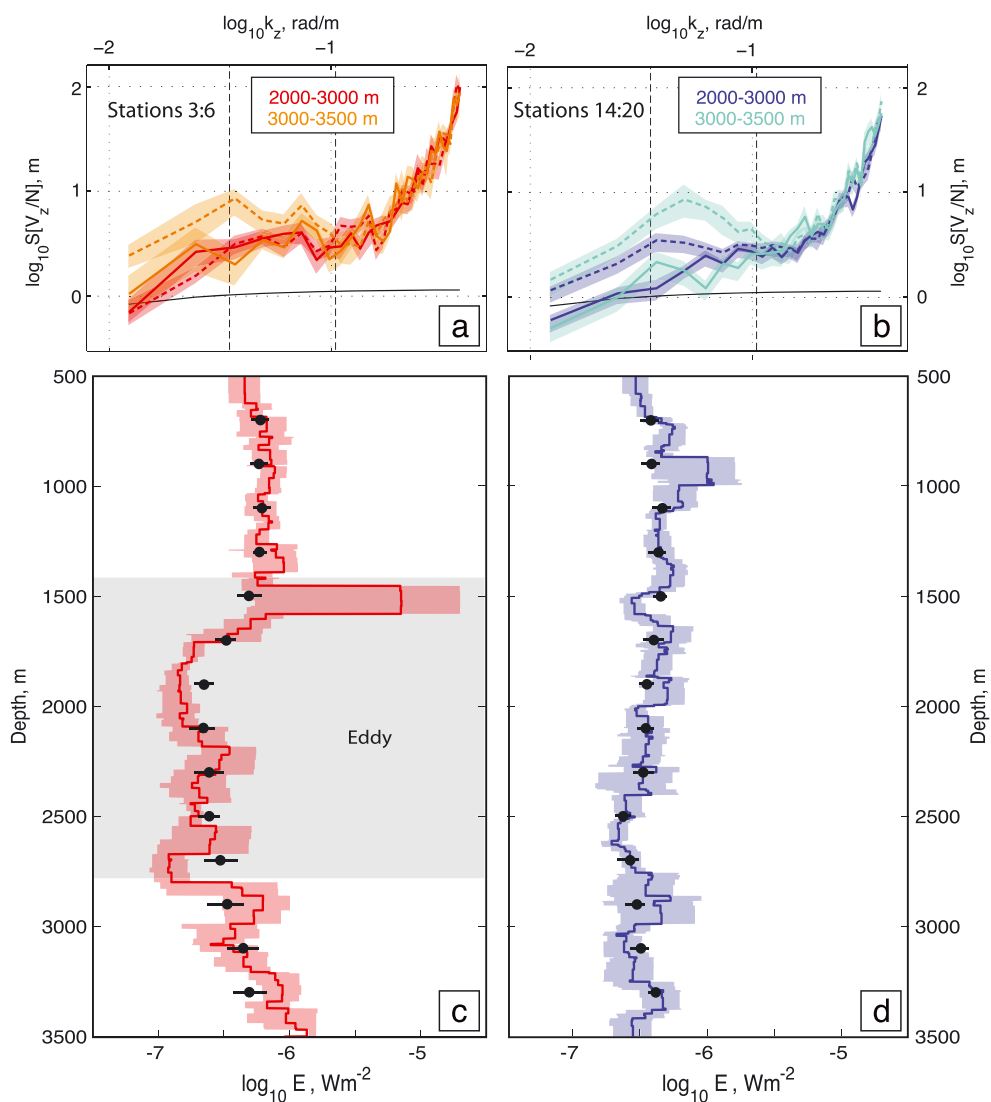
Figure 4. (a and b) Buoyancy normalized shear spectra for the eddy and noneddy stations, respectively, averaged into depth bins. Solid lines show CCW components (i.e., predominant downward energy propagation), and dashed lines show CW (i.e., predominant upward energy propagating) component. The vertical dashed lines show the vertical wavelength band (60–180 m) over which spectra are integrated for the calculation of shear variance. The shaded regions show the 95% confidence interval in mean values, calculated by bootstrapping, and the Garrett-Munk level is indicated by the black solid line. Note the enhancement in CCW compared with CW for depths >3000 m when the eddy is present. (c and d) Depth profiles of the wave energy flux, $E_f = C_{gz}(KE + APE)$ (black dots) and the microstructure-deduced dissipation rates multiplied by density and integrated over 1 m depth bins (solid line), $E_\epsilon = \int (1 + 0.2)\epsilon\rho \ dz$, for the eddy (Figure 4c) and noneddy (Figure 4d). The kinetic energy, KE, and available potential energy, APE, were deduced from LADCP and CTD data, respectively, over vertical wavelengths in the range 60–180 m (see *Sheen et al.* [2013] for details). The vertical group velocity, C_{gz}, is computed for a single wave using $(\omega^2 - f^2)(N^2 - \omega^2)/[\omega m(N^2 - f^2)]$, where the vertical wave number $m = 2\pi/\lambda_z$. We choose $\lambda = 100$ m, a value midway between the vertical integration limits of the energy spectra, and $\omega = 1.4 \ f$. The shaded regions and horizontal black lines show the 95% confidence interval in mean values.

The dominant mechanisms of internal wave generation in the ACC are the interaction of the wind with the sea surface (the waves generated in this case are characterized by a strongly inertial frequency content), the flow of deep geostrophic currents over topography (i.e., generating lee waves), and the generation of internal tides [*Waterman et al.*, 2012; *Sheen et al.*, 2013; *Brearley et al.*, 2013]. Therefore, for each model (noneddy and eddy), rays were emitted from two locations: at 500 m, with vertical wave number, $k_z > 0$, such that the wave initially propagates downward, and at 3499 m with $k_z < 0$, such that the initial propagation of the wave is upward. Several raypaths were computed, with initial vertical wavelengths varying between 10 m and 1000 m (typical of internal waves) and incident angles, α, varying between 0° and 180° (α represents the angle between the
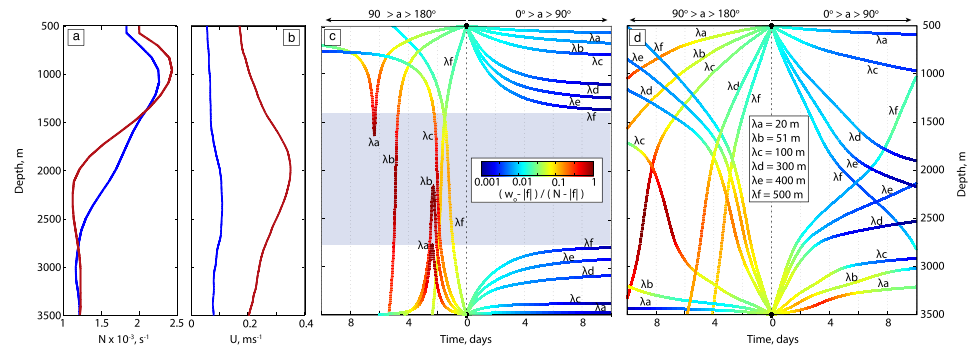
Figure 5. Ray tracing model inputs and results. (a) Input stratification profiles for eddy (red) and noneddy (blue) ray tracing models. (b) As for Figure 5a but for current speed depth profiles. (c) Computed ray paths for eddy model. Colors track the wave frequency, in relation to the local N and $|f|$: blue represents evolution toward a critical layer scenario (ω_o approaches f), while red indicates a turning point as ω_o reaches N. Initial vertical wavelengths, λ_z, for each raypath are marked. All rays are initiated at $\alpha = 45°$ (i.e., propagating in the same direction of the background flow, left-hand side of the panel) or at $\alpha = 135°$ (i.e., propagating against the background flow, right-hand side of the panel). The gray box highlights the region of the eddy core, where no internal waves approach a critical layer scenario. (d) As for Figure 5c but for the noneddy model.

initial raypath and the horizontal x axis such that for $0° < \alpha < 90°$ the rays will initially propagate in the same direction as the mean current and for $90° < \alpha < 180°$ the waves will propagate against the mean flow). All waves are emitted with horizontal wave number, $k_x = \cos(\alpha) \left[k_z^2 \left(\omega^2/f^2 - 1 \right) / \left(N_o^2/f^2 - \omega^2/f^2 \right) \right]^{1/2}$, where ω is the local wave frequency (a constant along the raypath), k_z the vertical wave number, N_o is the local N at the first time step, and for simplicity a constant $\omega/f = 1.4$, the average value at the wave initiation depths as computed from shear-to-strain ratios (see Figure 3c). The time evolution of internal wave characteristics was tracked using finite differencing, with the wave position, wave number, and frequency being updated on 10 min time steps. The model was run for a 10 day period.

We note that these simple ray tracing models are presented as a heuristic tool and are not intended to capture the full range of wave-mean flow interactions at play in such a complex system. For example, the models fail to account for the breakdown of the WKB analysis at critical layers [*Booker and Bretherton*, 1967; *Jones*, 1967], the consequences of using the WKB approximation in a background flow with relatively small horizontal length scales ($O(10 \text{ km})$) [*Olbers*, 1981; *Whitt and Thomas*, 2012], the assumption that the mean flow is 1-D and rectilinear [*Bühler and McIntyre*, 2005; *Polzin*, 2008], the potential for loss/gain of wave energy to the mean flow and/or a wave-induced effective viscosity [*Booker and Bretherton*, 1967; *Muller*, 1976; *Polzin*, 2010], the effect of f/N approaching 0.1 [e.g., *Gerkema and Exarchou*, 2008], the influence of the eddy rotation and the inclusion of the vorticity term in the ray tracing formulation [*Kunze et al.*, 1995], and double diffusive processes.

Despite these caveats, the models are useful in developing a broad intuition and visual illustration of plausible larger-scale effects of the eddy on internal wave propagation and breaking. Moreover, quantification of the wave energy flux and Richardson numbers in section 3.5 indicates that internal wave breaking by critical layer mechanisms, as suggested by the ray tracing exercise, is a plausible source of the observed dissipation surrounding the eddy.

5. Results

Despite the many raypaths computed, only a representative subset is illustrated here for clarity (Figures 5c and 5d). The raypaths are colored to represent the progressive change in the intrinsic frequency of the wave, ω_o, relative to $|f|$ and the local buoyancy frequency, N, along their path, which is a proxy for the behavior of the wave: blue represents evolution toward a critical layer scenario (ω_o approaches f), while red indicates a turning point as ω_o reaches N.

On comparing results from the two ray tracing models, the lack of critical layer interactions (and an associated lack of wave breaking) between 1400 m and 2800 m is immediately apparent when the eddy is present (Figure 5). This depth range corresponds very well to the region of suppressed mixing within the eddy core seen in the microstructure dissipation estimates (Figures 2 and 3). In contrast, critical layer interactions occur throughout the water column (for waves propagating into the current) in the noneddy case.

In the ray tracing model output, the presence of the eddy appears to deflect critical layer interactions into the region between the eddy base and the seabed and within a 400 m deep band above the eddy. Such interactions may explain the enhanced turbulent dissipation at the upper and lower eddy boundaries, as measured by the microstructure profilers. The critical layers seen at this location in the ray tracing calculations are also consistent with the lower ω/f (high shear-to-strain ratios) measured on the upper edge of the eddy (1000–1700 m; γ_n = 27.60–27.85 m^{-3}) as well as the rapid decrease in ω/f with height above the seabed between γ_n = 27.95 kg m^{-3} (2500 m) and γ_n = 28.10 kg m^{-3} (3500 m), compared to background levels (Figure 3).

For lee waves traveling against the current flow (likely the dominant direction of bottom sourced waves which tend to be phase locked to the topography), the ray tracing for the eddy model reveals that some waves are reflected within the eddy core (Figure 5c). For this set of waves (i.e., at the first time step, ω/f = 1.4, α=137.5°, and $\lambda_z < 51$ m), the turning point which occurs at $\omega_o = N$ is due to the influence of decreasing shear and a local minimum in N on the wave frequency. The waves for which ω_o remains less than N propagate through the eddy and emerge at around 1000 m where they subsequently progress toward a critical layer scenario. Downward propagating waves from the surface also tend to reflect at the eddy core. Due to the stronger stratification and weaker shear at 2000 m, no such turning points occur for the noneddy model. The reflection of internal waves within the eddy core closely matches the observed peak in ω/f at 27.88 kg m^{-3} (2000 m) associated with the presence of the eddy (Figure 3c). Moreover, these turning waves could explain the observed enhancement of downward energy propagation below the eddy and reduction of upward propagating energy above the eddy. Internal wave reflection by the eddy is likely to be less important for waves propagating down from the surface for two reasons: (1) the ray tracing indicates that the vertical wavelength criterion for reflection is lower for surface-sourced waves ($\lambda_z < 50$ m) and (2) surface-sourced waves are likely to have a more isotropic spread of wave directions (cf. lee waves skewed toward $\alpha > 90°$).

6. Conclusions

In this study, we have used an opportunistic set of hydrographic, current velocity, and microstructure measurements, along with ray tracing calculations, to investigate the effect of a subsurface, Southern Ocean eddy on local turbulent dissipation rates and internal wave propagation. The presence of the eddy suppresses turbulent kinetic energy dissipation within the eddy core while enhancing turbulent dissipation rates near the eddy upper and lower boundaries. A peak in the internal wave frequency content occurred at the center of the eddy, while a more inertial frequency content, suggesting evolution toward critical layer breaking, was observed along the eddy's upper and lower boundaries. In addition, a suppression of upward propagating internal wave energy above the eddy alongside an enhancement of downward propagating internal wave energy beneath the eddy was recorded. These observations are consistent with the predictions from a linear ray tracing model, which suggest that the middepth velocity maximum and stratification minimum associated with the eddy act to modify the evolution of propagating internal waves. Depending on their propagation direction relative to the background shear, the modeled internal waves either encounter a critical layer above and below the eddy or are reflected at the eddy core. The eddy may therefore act to deflect internal wave breaking from its own core into the surrounding waters. However, a more thorough investigation of the energy pathways between balanced mesoscale flow and fine-structure and microstructure variance is needed to provide a detailed interpretation of the observations.

Although the breaking internal waves surrounding the eddy will degrade the coherent nature of the vortical structure through turbulent dissipation, a simple calculation indicates that the ultimate eddy lifetime is set by isopycnal mixing processes. The eddy decay time due to isopycnal mixing, T_h, is given by $4R^2/K_h$, where R is the eddy radius and K_h the isopycnal diffusivity. Taking an eddy radius, R, of 20 km [*Brearley et al.*, 2014], and a typical K_h associated with this length scale of 10–100 m^2 s^{-1}, [*Ledwell et al.*, 1998; *McWilliams*, 1985; *Hibbert et al.*, 2009], T_h is around 1 month to 1 year. In comparison, the diapycnal eddy decay time, T_v, is of the order of tens of years: $T_v = H^2/K_\rho = H^2N^2/(0.2\epsilon)$ [*Osborn*, 1980], where $H = 1$ km is the thickness of the eddy core, $\epsilon = 10 \times 10^{-10}$ W kg^{-1} is the turbulent dissipation rate around the eddy core, and $N = 1 \times 10^{-3}$ s^{-1}.

Acoustically tracked floats and mooring data in the Drake Passage region indicate that middepth anticyclonic eddies occur regularly and play a major role in the disintegration of the deep boundary current that flows along the southwestern continental slope of South America [*Brearley et al.*, 2014]. This study suggests that these persistent, ubiquitous features also significantly modify the local small-scale turbulence field along

their path through some flavor of wave-mean flow interactions, contributing to the patchy nature of oceanic turbulent dissipation and diapycnal mixing.

References

Armi, L., D. Hebert, N. Oakey, J. Price, P. L. Richardson, T. Rossby, and B. Ruddick (1988), The history and decay of a Mediterranean salt lens, *Nature*, *333*, 649–651.

Bray, N. A., and N. P. Fofonoff (1981), Available potential energy for MODE eddies, *J. Phys. Oceanogr.*, *11*, 30–46.

Booker, J. R., and F. P. Bretherton (1967), The critical layer for internal gravity waves in a shear flow, *J. Fluid Mech.*, *27*(3), 513–539.

Brearley, J. A., K. L. Sheen, A. C. Naveira Garabato, D. A. Smeed, and S. Waterman (2013), Eddy-induced modulation of turbulent dissipation over rough topography in the Southern Ocean, *J. Phys. Oceanogr.*, *43*, 2288–2308.

Brearley, J. A., K. L. Sheen, A. C. Naveira Garabato, D. A. Smeed, K. G. Speer, A. M. Thurnherr, M. P. Meredith, and S. Waterman (2014), Deep boundary current disintegration in Drake Passage, *Geophys. Res. Lett.*, *41*, 121–127, doi:10.1002/2013GL058617.

Bühler, O., and M. E. McIntyre (1999), On shear-generated gravity waves that reach the mesosphere. Part II: Wave propagation, *J. Atmos. Sci.*, *56*, 3764–3773.

Bühler, O., and M. E. McIntyre (2005), Wave capture and wave-vortex duality, *J. Fluid Mech.*, *534*, 67–95.

Forryan, A., J. T. Allen, E. Edhouse, B. Silburn, K. Reeve, and E. Tesi (2012), Turbulent mixing in the eddy transport of Western Mediterranean intermediate water to the Alboran Sea, *J. Geophys. Res.*, *117*, C09008, doi:10.1029/2012JC008284.

Gerkema, T., and E. Exarchou (2008), Internal wave properties in weakly stratified layers, *J. Mar. Res.*, *66*(5), 617–644.

Hibbert, A., H. Leach, V. Strass, and B. Cisewski (2009), Mixing in cyclonic eddies in the Antarctic Circumpolar Current, *J. Mar. Res.*, *67*, 1–23, doi:10.1357/002224009788597935.

Jones, W. L. (1967), Propagation of internal gravity waves in fluids with shear flow and rotation, *J. Fluid Mech.*, *30*, 439–448.

Kunze, E., R. W. Schmitt, and J. M. Toole (1995), The energy balance in warm-core ring's near inertial critical layer, *J. Phys. Oceanogr.*, *25*, 942–957.

Ledwell, J. R., A. J. Watson, and C. S. Law (1998), Mixing of a tracer in the pycnocline, *J. Geophys. Res.*, *103*, 21,499–21,529.

Lighthill, M. J. (1978), *Waves in Fluids*, 504 pp., Cambridge Univ. Press, Cambridge, U. K.

Marshall, J., and K. Speer (2012), Closure of the meridional overturning circulation through Southern Ocean upwelling, *Nat. Geosci.*, *5*, 171–180.

McDowell, S. E., and H. Rossby (1978), Mediterranean water: An intense mesoscale eddy off the Bahamas, *Science*, *202*, 1085–1087.

McWilliams, J. C. (1985), Submesoscale, coherent vortices in the ocean (1985), *Rev. Geophys.*, *23*, 165–182.

Muller, P. (1976), On the diffusion of momentum and mass by internal gravity waves, *J. Fluid Mech.*, *77*(4), 789–823.

Olbers, D. J. (1981), Propagation of internal waves in a geostrophic current, *J. Phys. Oceanogr.*, *11*, 1224–1233.

Orsi, A. H., T. Whitworth III, D. Worth, and W. D. Nowlin Jr. (1995), On the meridional extent and fronts of the Antarctic Circumpolar Current, *Deep Sea Res., Part I*, *42*, 641–673.

Osborn, T. R. (1980), Estimates of the local rate of vertical diffusion from dissipation estimates, *J. Phys. Oceanogr.*, *10*, 83–89.

Polzin, K. L. (2008), Mesoscale eddy-internal wave coupling. Part I: Symmetry, wave capture, and results from the Mid-Ocean Dynamics Experiments, *J. Phys. Oceanogr.*, *38*, 2556–2574.

Polzin, K. L. (2010), Mesoscale eddy-internal wave coupling. Part II: Energetics and results from POLYMODE, *J. Phys. Oceanogr.*, *40*, 789–801.

Polzin, K. L., A. C. Naveira Garabato, T. N. Huusen, B. M. Sloyan, and S. N. Waterman (2014), Finescale parameterizations of turbulent dissipation, *J. Geophys. Res. Oceans*, *119*, 1383–1419, doi:10.1002/2013JC008979.

Richardson, P., A. Bower, and W. Zenk (2000), A census of Meddies tracked by floats, *Prog. Oceanogr.*, *45*, 209–250.

Sheen, K. L., N. J. White, and R. W. Hobbs (2009), Estimating mixing rates from seismic images of oceanic structure, *J. Geophys. Res.*, *36*, L00D04, doi:10.1029/2009GL040106.

Sheen, K. L., et al. (2013), Rates and mechanisms of turbulent dissipation and mixing in the Southern Ocean: Results from the Diapycnal and Isopycnal Mixing Experiment in the Southern Ocean (DIMES), *J. Geophys. Res. Oceans*, *118*, 2774–2792, doi:10.1002/jgrc.20217.

Waterman, S., K. L. Polzin, and A. C. Naveira-Garabato (2012), Internal waves and turbulence in the Antarctic Circumpolar Current, *J. Phys. Oceanogr.*, *43*, 259–282.

Watson, A. J., J. R. Ledwell, M. Messias, B. A. King, N. Mackay, M. P. Meredith, B. Mills, and A. C. Naveira Garabato (2013), Rapid cross-density ocean mixing at mid-depths in the Drake Passage measured by tracer release, *Nature*, *501*, 408–413, doi:10.1038/nature12432.

Well, R., W Roether, and D. P. Stevens (2003), An additional deep water mass in Drake Passage as revealed by ^{3}He data, *Deep Sea Res., Part I*, *50*, 1079–1098.

Whitt, D. B., and L. N. Thomas (2012), Near-inertial waves in strongly baroclinic currents, *J. Phys. Oceanogr.*, *43*, 706–725.